Materials Science & Engineering A 880 (2023) 145211

Contents lists available at ScienceDirect

Materials Science & Engineering A

journal homepage: www.elsevier.com/locate/msea

Incorporating dynamic recrystallization into a crystal plasticity model for high-temperature deformation of Ti-6Al-4V

Arunabha M. Roy [a,b,*], Raymundo Arróyave [b,c], Veera Sundararaghavan [a]

[a] Aerospace Engineering, University of Michigan, Ann Arbor, MI 48109, USA
[b] Department of Materials Science and Engineering, Texas A&M University, 3003 TAMU, College Station, TX 77843, USA
[c] Department of Mechanical Engineering, Texas A&M University, 3003 TAMU, College Station, TX 77843, USA

ARTICLE INFO

Keywords:
Crystal Plasticity
Dynamic Recrystallization
ICME
(α+ β)-Titanium (Ti) Alloys
Flow Stress–Strain response
Texture Prediction

ABSTRACT

During hot deformation of ($\alpha + \beta$) titanium alloys, the simultaneous action of strain and temperature in the ($\alpha + \beta$) regime facilitates dynamic recovery, dynamic recrystallization (DRX), and phase transformations via non-equilibrium paths. DRX is manifested in the form of fine recrystallized α or β grains. In the present study, a two-phase crystal plasticity finite element framework (CP-DRX) has been developed which incorporates DRX kinetics into the crystal plasticity (CP) model to predict the flow characteristics of Ti-6Al-4V alloys during thermo-mechanical processing. The CP slip system parameters, as well as elastic properties from both α and β phases of Ti, are calibrated for different strain rate conditions. An EBSD-informed two-phase microstructure representation has been utilized in the CP-DRX framework to explore the time-dependent evolution of DRX microstructure and crystal orientation for different strain rate conditions. The proposed CP-DRX can capture the evolution of crystal orientation and plastic flow stress–strain response of polycrystalline Ti-6Al-4V during the deformation process. Furthermore, the proposed model is able to capture the softening behavior, observed in average stress–strain response from experiments performed using a Gleeble thermomechanical simulator and predict the recrystallization texture.

1. Introduction

Two phases ($\alpha + \beta$)-type titanium (Ti) alloys are commercially attractive in naval, aerospace, and biomedical fields due to their superior mechanical strength, high-temperature resistance, good formability, and excellent corrosion resistance capability [1,2]. In this regard, hot forming is an important process for manufacturing complex shapes of these alloys. Due to severe plastic deformation during hot forming, different grains undergo complex microstructural evolution which in turn, can significantly influence the deformation behavior and mechanical properties of Ti alloys [3]. Additionally, the hot deformation process in the sub/near- transus ($\alpha + \beta$) and/or super-transus regimes can facilitate dynamic recrystallization (DRX) which is a typical phenomenon observed during microstructural evolution of ($\alpha + \beta$) dual phase Ti alloys [4,5]. Several experimental works have been geared towards the investigation of DRX during the hot deformation process in titanium alloys [6,7] demonstrating the appearance of newly equiaxed α [8–10] and β grains [11,12].

During plastic deformation, new strain-free grains are formed that can significantly affect the mechanical response of the materials. Generally, DRX occurs during plastic deformation at elevated temperatures associated with softening mechanism that restores the ductility of the polycrystalline Ti [6,7]. The DRX mechanism can be characterized in three distinct forms including discontinuous, continuous, and geometric DRX [5]. In general, discontinuous DRX is associated with nucleation of DRX grain and grain growth; continuous DRX occurs during dynamic recovery when the formation of new DRX grain structures with low-angle grain boundaries take place and evolve into low-angle grain boundaries [4]; geometric DRX is accompanied by the serration of grain boundaries and significant grain refinement [5]. Typically, the DRX mechanism initiates upon exceeding specific threshold values, such as a critical strain [3] or critical dislocation density [13], accompanied by the nucleation of new grains, preferentially on the grain boundaries at a strain rate that is dependent on the working temperature. DRX results in grain growth, dislocation accumulation, texture formation, twin structures, and serrated boundaries during deformation which reduces systemic energy and ultimately affects the hot working behavior [14–16]. This is especially the case for complex forming processes such as linear friction welding (LFW) in Ti-alloys [17–19].

In the context of plastic deformation and microstructure evolution of heterogeneous materials, the approach of mesoscale mechanical

* Corresponding author at: Aerospace Engineering, University of Michigan, Ann Arbor, MI 48109, USA.
E-mail addresses: royam@tamu.edu, arunabhr.umich@gmail.com (A.M. Roy).

https://doi.org/10.1016/j.msea.2023.145211
Received 19 March 2023; Received in revised form 18 May 2023; Accepted 26 May 2023
Available online 1 June 2023

models such as crystal plasticity (CP) is a powerful method equipped with physics-based constitutive theories [20–23] to link the mechanical properties of materials with the evolution of subgrain morphology as well as recrystallized grains under an applied stress or displacement field [20]. In the last decades, several studies on dual-phase titanium alloys, in particular, Ti-6Al-4V alloys have been performed utilizing CP models [24–27] considering both the α and β phases of the Ti [28–32]. More recently, the CP model has been extended to study the cyclic shear loading [33] and the effect of orientation and morphology of the α-Ti and β-Ti phases of Ti-6Al-4V alloys on time-dependent cyclic loading [34]. Additionally, diffuse interface approaches such as phase-field (PF) models have been integrated with the CPFE framework to capture grain boundary sliding, migration of grain structure, the effect of strain rate on DRX and grain growth [35–37]. Hence, the material process modeling approachs have shown to be effictive tool for investigating mechanical response in heterogeneous materials undergoing microstructure and mechanical property evolution during material fabrication and operation [38,39].

In the current study, the presence of DRX has been observed in Electron Back Scatter Diffraction (EBSD) images of two-phase Ti-6Al-4V alloys during different strain rates at elevated temperatures. While the different strain rates influence the DRX process, the DRX itself affects subsequent deformation due to newly generated grains, new grain orientations, dislocation density reduction, and evolution of the recrystallized grains. The respective influence of the plastic deformation and the DRX take place simultaneously and interactively. Hence, a proper CP framework to account for DRX phenomena is important to capture stress–strain responses. Since the α phase and the β phase of Ti have different crystallographic structures, proper calibration of the corresponding CP parameters at different strain rates is important, particularly at elevated temperature, to obtain the correct deformation behavior in heterogeneous ($\alpha + \beta$)- titanium alloys. Moreover, the DRX mechanism contains recrystallization and grain growth kinetics that depends on peak strain and the DRX volume fraction [40,41]. However, a consistent CP framework accounting for DRX kinetics has yet to be systematically addressed in the current state-of-the-art modeling approaches for complex heterogeneous materials, in particular, $\alpha + \beta$ titanium alloys. Thus, in order to develop a comprehensive integrated computational materials engineering (ICME) [38,42] capability for the hot forming of titanium alloys, it is important to quantify the kinetics of DRX during the thermo-mechanical process to capture the stress–strain response and finally predict the mechanical behavior of the materials [3].

In order to address the aforementioned challenges, in this paper, we present a crystal plasticity framework accounting for DRX kinetics (CP-DRX) to predict the flow characteristic during thermomechanical processing for Ti-6Al-4V. The optimum slip system parameters, as well as elastic properties from both α and β phases of Ti, are calibrated from the experimental stress–strain path by solving an inverse optimization problem through crystal plasticity simulations for different strain rates at elevated temperatures. Furthermore, different kinetic parameters associated with the DRX mechanism have been calibrated directly from experimental Ti-6Al-4V data and integrated into the CP model. In the proposed CP-DRX model, a realistic EBSD-informed two-phase microstructural representation has been included to explore the time-dependent evolution of DRX microstructure and texture for different strain rate conditions. Additionally, the flow stress–strain behavior predictions from CP-DRX for different strain rates have been discussed and directly compared with experimental results. The simulation results are in good agreement with experimental observations. It is found that the proposed CP-DRX model can capture the softening in experimental stress–strain behavior that occurs during hot deformation and predict the final recrystallized texture of the deformed microstructure. The rest of the paper is organized as follows: Section 2 describes the material and experimental procedure for Ti-6Al-4V; Section 3 introduces the crystal plasticity finite element model; calibration of slip system parameters for different strain rate conditions has been described in Section 4; experimental quantification of kinetic parameters of DRX has been discussed in Section 5; Section 6 deals with the relevant findings and discussion of the proposed framework. Finally, the conclusions and future prospects of the current work have been discussed in Section 7.

2. Material and experimental procedure

The material used for the current study is a Ti-6A-4V alloy sheet specimen which was received in the form of a plate in mill-annealed condition. Compression cylinders were machined using electro-discharge machining (EDM) to form cylindrical coupons of size 10 mm diameter × 15 mm length, according to ASTM E-9. Hot compression experiments were performed using a Gleeble 3500 Hydrawedge. Thermocouples were attached to the center of the samples to facilitate temperature measurements. Tantalum foils and nickel paste were used between the flat cylindrical surfaces and tungsten carbide anvil faces. This reduces friction effects and maintains good contact between the anvils and the specimen, which is critical for maintaining a uniform temperature across the specimen. A high voltage is passed through the anvil-specimen assembly which produces nearly instantaneous heating of the sample using resistive heating. The recrystallization and transformation of the as-received microstructure are analyzed using Scanning Electron Microscopy (SEM)/Back Scattered Electron (BSE) imaging and quantified using electron backscatter diffraction (EBSD)/Grain Orientation Spread (GOS) technique. In both categories of experiments, compression tests, and annealing is performed at the sub, near, and super transus temperatures. The transus temperature for Ti-6A-4V is 995 °C. The hot compression experiments reported in this paper were performed at 800 °C. A heating rate of 100 °C/s is a compromise between values that are representative of the LFW process and the limitations of resistive heating. A dwell time of 10 s is allowed prior to the deformation of the sample at different strain rates. The final strain of 0.8 is typical of LFW processes. The average global stress–strain response is measured from the Gleeble. Deformed samples were sectioned, and polished using standard metallography and colloidal silica to facilitate characterization via EBSD. Furthermore, for the deformed samples, 12–15 h of vibratory polish in a colloidal silica slurry using a VibroMet was performed. For our present study, strain-controlled deformation experiments were performed at two different strain rates (0.001 and 0.1 s^{-1}), where the final strain values (0.5, 0.8) were specified. Finally, the engineering curves obtained from the uniaxial compression tests were converted into the true stress–strain curves. After deformation, the change of microstructure and property of the deformed specimens were observed using the EBSD technique as shown in Fig. 1 where CD and TD represent compression and transverse direction, respectively. A voltage of 25 kV and beam intensity 15–18 with a 2 × 2 binning is used for EBSD characterization. The field of view (FOV) for EBSD analysis is in the range of 200–300 μm with a step size of 0.3–0.5 μm. The step sizes and FOV are optimized to facilitate the effective resolution of the finer recrystallized grains. Additionally, X-ray Diffraction (XRD) analysis has been performed along with image processing of BSE and optical images. Fig. 2-(a) shows the XRD analysis results at different hold times for a sample deformed to 25% at room temperature and annealed at 800 °C. Fig. 2-(b) shows the β volume fraction evolution with respect to hold time, and figures Fig. 2-(c–f) show the BSE images with the presence of both α (gray) and β (white) phases. The volume fraction of the β regions is determined using Image J and applying appropriate thresholding to distinguish it from the gray α phase. The kinetics of static recrystallization and phase transformation at sub-transus temperatures of 800 °C for different annealing times are presented in Fig. 2-(g–j) where the circles represent experimental data.

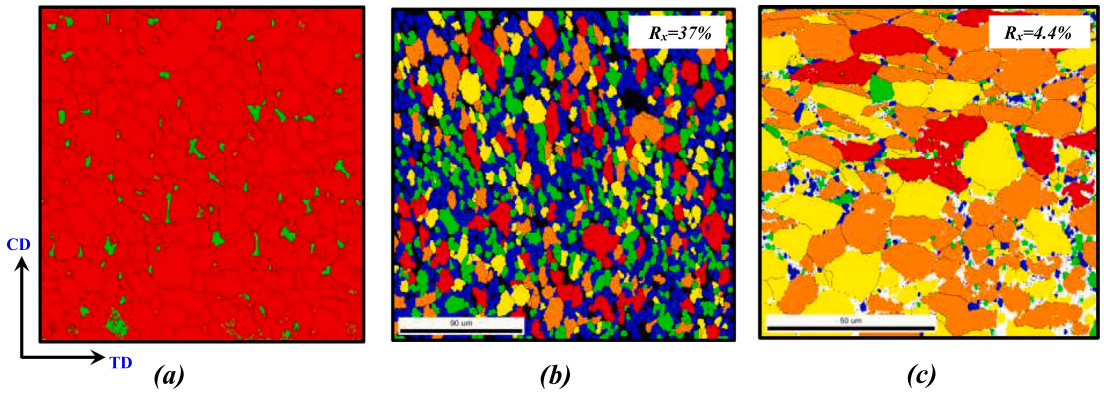

Fig. 1. (a) Experimental EBSD inverse pole figure image showing as received microstructure with a phase fraction of 95% HCP α-Ti (red) and 5% BCC β-Ti (green) in parent Ti-6Al-4V sample at ambient temperature; experimental EBSD images showing the emergence of recrystallized grain (blue) during deformation process for final strain at temperature; $T = 800$ °C for different strain rates (b) $\partial\varepsilon/\partial t = 0.001$ s^{-1} at $\varepsilon_f = 0.5$; (c) $\partial\varepsilon/\partial t = 0.1$ s^{-1} at $\varepsilon_f = 0.80$. R_x represents the volume fraction of recrystallized grains. (For interpretation of the references to color in this figure legend, the reader is referred to the web version of this article.)

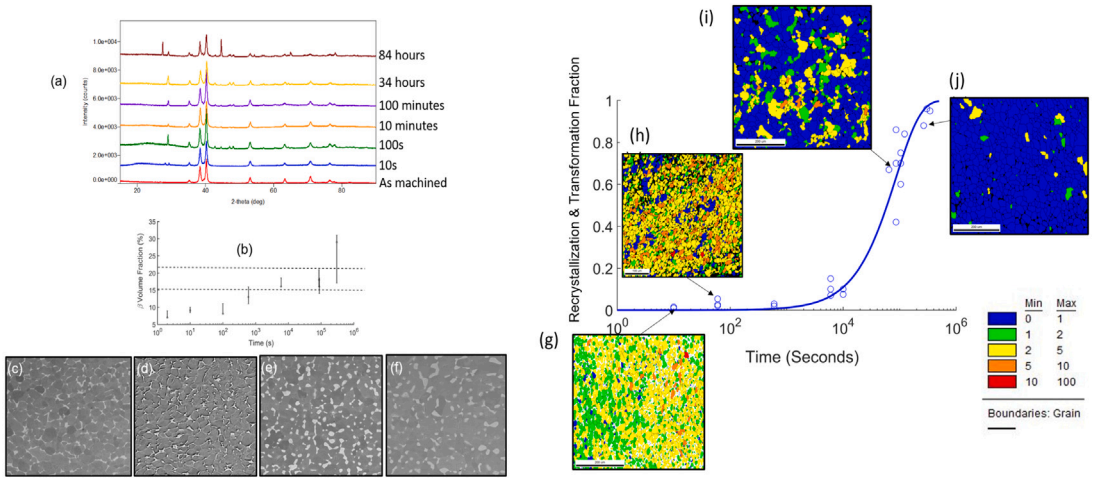

Fig. 2. (a) XRD analysis of Ti-6A-4V deformed to 25% at room temperature, followed by annealing at 800 °C for the hold times indicated, (b) beta fraction evolution with time at 800 °C, and BSE images for (c) as received, (d) 100 s, (e) 34 h, and (f) 84 h where recrystallization and transformation kinetics during annealing at 800 °C showing (a)–(d) GOS maps corresponding to different hold times surround the plot.

3. Crystal plasticity finite element model

For the current work, a rate-independent single-crystal plasticity finite element model (CPFE) [43–45] has been employed to obtain the distribution of macroscopic strain on the polycrystal Ti-6Al-V alloys. Additionally, the evolution of DRX grain growth and texture distribution has been explored for different strain rate conditions during the hot deformation process.

In the CPFE formulation, the crystal consisting of $\alpha = 1, \ldots, N$ slip systems which can be represented by pairs of orthonormal vectors ($\boldsymbol{m}^\alpha$, $\boldsymbol{n}^\alpha$). In the deformed configuration, unit vectors $\boldsymbol{m}^\alpha$ and $\boldsymbol{n}^\alpha$ are the slip direction and slip plane normal of the slip system, respectively. In this theory, the accommodation of plastic flow has been assumed to take place through slip on specified slip systems. In the constitutive equations, the deformation gradient tensor $\boldsymbol{F}$ can be expressed after multiplicative decomposition as: $\boldsymbol{F} = \boldsymbol{F}^e\boldsymbol{F}^p$, where $\boldsymbol{F}^e$ and $\boldsymbol{F}^p$ represent the elastic and the plastic part of $\boldsymbol{F}$, respectively. For the kinematics of single-crystal slip, the applied deformation can be attributed to two independent deformation mechanisms, i.e, elastic distortion of the crystal lattice and pure shear due to plastic slip. Thus, macroscopic velocity gradient tensor $\boldsymbol{L}$ can be expressed after additive decomposition as $\boldsymbol{L} = \boldsymbol{L}^e + \boldsymbol{L}^p$, where $\boldsymbol{L}^e$ and $\boldsymbol{L}^p$ denote the elastic and plastic parts of $\boldsymbol{L}$, respectively. To connect macroscopic response to microscopic mechanisms of deformation in the CPFE model, the plastic part of the velocity gradient $\boldsymbol{L}^p$ can be linked to shear deformation induced by crystallographic slip on multiple slips. Assuming deformation takes place through dislocation glide, the evolution of the plastic flow can be expressed as

$$\boldsymbol{L}^p = \dot{\boldsymbol{F}}^p(\boldsymbol{F}^p)^{-1} = \sum_\alpha \dot{\gamma}^\alpha \boldsymbol{S}_0^\alpha sign(\tau^\alpha) \tag{1}$$

where $\boldsymbol{L}^p$ represents the macroscopic rate of plastic distortion, $\dot{\gamma}^\alpha$ is the plastic shearing rate on the α^{th} slip system, and $\boldsymbol{S}_0^\alpha = \boldsymbol{m}^\alpha \otimes \boldsymbol{n}^\alpha$ is the Schmid tensor. The resolved shear stress $\boldsymbol{\tau}^\alpha$ on the α^{th} slip system can be expressed as

$$\boldsymbol{\tau}^\alpha = \bar{\boldsymbol{T}} \cdot \boldsymbol{S}_0^\alpha \tag{2}$$

Here, $\bar{\boldsymbol{T}}$ is the Cauchy stress tensor which can be expressed as follows:

$$\boldsymbol{T} = \left(\frac{1}{\det \boldsymbol{F}_r}\boldsymbol{P}_r\boldsymbol{F}_r^T\right); \quad s^\alpha > 0 \tag{3}$$

Where s^α is the slip resistance of α^{th} slip system. Subsequently, the Green elastic strain measure can be expressed as $\bar{\boldsymbol{E}}^e = \frac{1}{2}\left(\boldsymbol{F}^{eT}\boldsymbol{F}^e - \boldsymbol{I}\right)$ which has been defined on the unstressed, plastically deformed configuration. The conjugate stress measure can then be defined as $\bar{\boldsymbol{T}} = \det\boldsymbol{F}^e(\boldsymbol{F}^e)^{-1}\boldsymbol{T}(\boldsymbol{F}^e)^{-T}$ where $\boldsymbol{T}$ is the Cauchy stress for the crystal in the sample reference frame. The constitutive relation, for stress, is given by $\bar{\boldsymbol{T}} = \bar{\boldsymbol{C}}\left[\bar{\boldsymbol{E}}^e\right]$. For the rate-independent CPFE model, the yield surface

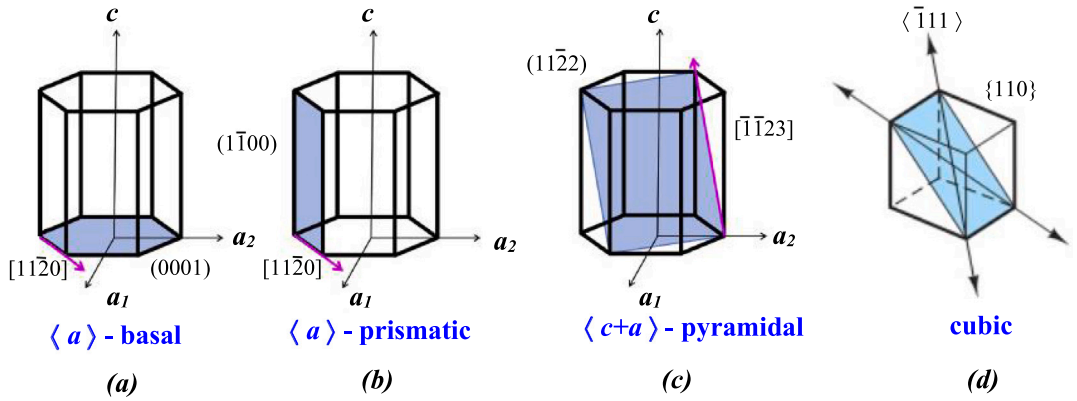

Fig. 3. Active slip systems in (a, b, c) HCP α-Ti; (d) BCC β-Ti at elevated temperature; $T = 800$ °C.

corresponds to α^{th} slip system can be expressed as :

$$f^{\alpha} = |\tau^{\alpha}| - s^{\alpha} \tag{4}$$

The slip will occur on α^{th} slip system if $|\tau^{\alpha}| > s^{\alpha}$. For inactive slip systems, $|\tau^{\alpha}|$ cannot overcome the critical value of s^{α} (i.e., $|\tau^{\alpha}| < s^{\alpha}$ or $|\tau^{\alpha}| = s^{\alpha}$). For such cases, the trial stress rate remains inside the yield surface. However, for $|\tau^{\alpha}| > s^{\alpha}$ the trial stress rate remains exterior of the yield surface and the corresponding slip system became potentially active to slip. This results in $\dot{\gamma}^{\alpha} \geq 0$. The aforementioned conditions satisfy the Karush–Kuhn–Tucker (KKT) consistency conditions in flow plasticity theory. Furthermore, the evolution of slip resistance s^{α} for α^{th} slip system can be expressed as:

$$\dot{s}^{\alpha}(t) = \sum_{\beta} h^{\alpha\beta}\dot{\gamma}^{\beta},\ s^{\alpha}(0) = s_0^{\alpha} \tag{5}$$

Eq. (5) is the hardening law for the slip resistance s^{α}; $h^{\alpha\beta}$ is the hardening moduli which defines the variation of slip resistance for slip system α due to the slip rate on slip system β. Considering the combined effect of work hardening and recovery, $h^{\alpha\beta}$ can be expressed as power-law relationship as follows:

$$\begin{aligned} h^{\alpha\beta} &= h_o^{\beta}\left[1 - \frac{s^{\beta}(t)}{s_s^{\beta}}\right]^{a^{\beta}} \quad \text{if } \alpha = \beta \text{ (coplanar systems)} \\ &= h_o^{\beta} q\left[1 - \frac{s^{\beta}(t)}{s_s^{\beta}}\right]^{a^{\beta}} \quad \text{if } \alpha \neq \beta \text{ (non-coplanar systems)} \end{aligned} \tag{6}$$

where h_o^{β} indicates the hardening parameter for slip system β; q denotes the latent hardening ratio; s_s^{β} represents the slip resistance of slip system β at hardening saturation; a^{β} is a material constant governing the sensitivity of the hardening moduli to the slip resistance for a particular slip system.

4. Calibration of slip system parameters for Ti-6Al-4V at elevated temperature

Polycrystalline Ti-6Al-4V is a heterogeneous alloy with two distinctly different phases which include hexagonal close-packed (HCP) α-Ti and body-centered cubic (BCC) β-Ti. Due to the difference in the crystallographic structure of these two phases, the slip systems for dislocation are distinct which leads to different plastic deformation modes [46,47]. Since, independent slip systems of the (BCC) β-phase are relatively less compared to (HCP) α-phase, hence, plastic deformation characteristic in α-phase is much more complex than β-phase in Ti-6Al-4V during hot deformation process [46,47]. Thus, for the proper calibration of CP slip system parameters, it is important to identify predominant active slip systems for both α and β-Ti at the elevated temperature. To this end, different slip system parameters corresponding to the CP model for both α and β-phases of Ti have been directly calibrated from experimental flow stress–strain curve for different strain rate conditions at temperature $T = 800$ °C. During calibration, design variables have been determined by optimizing the value of various active slip system parameters. In general, HCP α-Ti predominately display easy $\langle a \rangle$ slip, either on the basal or prismatic plane [46–48]. In pure HCP-Ti, the three main observed slip systems include three equivalent basal $\{0001\}\langle 11\bar{2}0\rangle$, three equivalent prismatic $10\bar{1}0\langle 11\bar{2}0\rangle$, and six equivalent pyramidal $10\bar{1}1\langle 11\bar{2}0\rangle$ slip systems [46,47]. The aforementioned slip systems share a common $\langle 11\bar{2}0\rangle$ or $\langle a\rangle$ slip direction. As shown in Fig. 3-(a, b), this slip has been denoted as $\langle a\rangle$-slip on basal, prismatic, and pyramidal slip systems. In addition, other slip modes such as slips on pyramidal planes with $\langle 11\bar{2}3\rangle$ or $\langle c + a\rangle$ slip or twinning deformation modes are required in the HCP system to accommodate strain parallel to c-axis. More importantly, at high temperature, three equivalent basal $\{0001\}\langle 11\bar{2}0\rangle$, three equivalent prismatic $10\bar{1}0\langle 11\bar{2}0\rangle$ and six equivalent pyramidal planes with $\langle 11\bar{2}3\rangle$, or $\langle c+a\rangle$ slip system are predominantly active [49,50]. Therefore, these three slip systems are included in the CP model as shown in Fig. 3-(a–c). At high temperatures, twinning slip systems are not activated for HCP-Ti [46,48], and thus, it has been excluded in our CP model. On the other hand, twelve equivalent $\{110\}\langle 111\rangle$ and twelve equivalent $\{112\}\langle 111\rangle$ slip systems are included in the CP model for the deformation behavior of BCC β-Ti as shown in Fig. 3-(d). Additionally, the yield stress of recrystallized grains (σ_Y^R) has been considered as an additional design parameter in our CP model to capture softening behavior of flow stress during the hot deformation process. The value of σ_Y^R depends on the strain rate and temperature. Moreover, it can be different in the α and β phases of newly recrystallized (DRX) grains. Thus, for different strain rate conditions, it is important to calibrate σ_Y^R from the experimental flow stress–strain curve. For simplicity, in the current framework, σ_Y^R has been assumed to be the fraction of macroscopic yield stress σ_Y for a particular strain rate that reduces additional fitting parameters in the CP model. We found that such a simplified assumption is quite effective to capture experimental flow stress response, in particular, softening behavior of the flow stress–strain curve during the hot deformation process (see Section 6.4).

For the calibration of slip system parameters in Ti-6Al-4V at elevated temperature, an ODF-based CP model has been utilized where the optimum slip system parameters are obtained by employing an inverse algorithm [51]. The main objective of the calibration process is to fit experimental flow stress curve characteristics in the CP model for various strain rates, considering an initial representative sample with random grain orientation (see Section 6.1). During the optimization procedure, several design variables including three slip system parameters (s_0^{α}, h_0^{α}, s_s^{α} and a^{α}) for three different slip systems taken into consideration for HCP α-Ti. These slip systems are basal $\langle a\rangle$, prismatic $\langle a\rangle$, pyramidal $\langle c+a\rangle$. For BCC β-Ti, four slip system parameters (s_0^{β}, h_0^{β}, s_s^{β} and a^{β}) of the two slip systems $\{110\}\langle 111\rangle$ and $\{112\}\langle 111\rangle$ have been

Table 1
Optimum slip system parameters of α-Ti at 800 °C for different strain rates.

Slip System	$\partial\varepsilon/\partial t$ (s^{-1})	s_0^α (MPa)	h_0^α (MPa)	s_s^α (MPa)	a^α
Basal $< a >$	0.001	27.45	355.50	68.63	1.38
	0.1	68.25	365.50	170.63	1.38
Prismatic $< a >$	0.001	27.45	355.50	68.63	1.38
	0.1	68.25	365.50	170.63	1.38
Pyramidal $< c+a >$	0.001	137.23	355.50	343.07	1.38
	0.1	341.25	365.50	853.13	1.38

Table 2
Optimum slip system parameters of β-Ti at 800 °C for different strain rates.

Slip System	$\partial\varepsilon/\partial t$ (s^{-1})	s_0^β (MPa)	h_0^β (MPa)	s_s^β (MPa)	a^β
Cubic $\{110\} < 111 >$	0.001	45.75	355.50	114.38	2.16
	0.1	113.75	365.50	284.38	2.16
Cubic $\{112\} < 111 >$	0.001	45.75	355.50	114.38	2.16
	0.1	113.75	365.50	284.38	2.16

considered. For further simplification of the calibration process, it has been assumed that the magnitude of s_0^α and s_s^α of the pyramidal $\langle c+a \rangle$ slip system should be higher (approximately in between three to five times) than the s_0^α value of the basal $\langle a \rangle$ slip system [48]. Additionally, the values of h_0^α and a^β have been assumed to be equal for all slip systems. Furthermore, $\sigma_Y^R = k(\partial\varepsilon/\partial t, \theta)\,\sigma_Y$ has been considered. Here, $k < 1$ is an additional calibration parameter that depends on strain rate and temperature. For a specific strain rate and temperature, the value of k is calibrated from the softening characteristic of the experimental flow stress–strain response. For strain rates $\partial\varepsilon/\partial t = 0.001$ and $\partial\varepsilon/\partial t = 0.1$, the optimized value of k is found to be $k = 0.82$ and $k = 0.86$, respectively at $\theta = 800$ °C. Finally, optimum slip system parameters for both α-Ti and β-Ti are calibrated through experimental compression stress–strain data as shown in Table 1 and Table 2, respectively. The elastic parameters of β-Ti (BCC monocrystal) are collected from [52] as: $C_{11} = 97.7$ GPa, $C_{12} = 82.7$ GPa, $C_{44} = 37.5$ GPa, and, whereas, for β-Ti (HCP monocrystal) from [53] as : $C_{11} = C_{22} = 175$ GPa, $C_{12} = 88.7$ GPa, $C_{13} = C_{23} = 62.3$ GPa, $C_{44} = C_{55} = 62.2$ GPa, and $C_{66} = (C_{11} - C_{12})/2$. The calibrated CP-DRX model has been validated against experimental R_x value and pole figures for different strain rate conditions.

5. Experimental quantification of kinetic parameters of DRX

In the proposed CP-DRX framework, DRX kinetics has been integrated into the CP model. Different kinetic parameters associated with the DRX mechanism have been calibrated directly from experimental Ti-6Al-4V data. In the proposed model, when the strain exceeds a critical value ε_c, DRX process begins accompanied by the nucleation and grain growth during hot deformation [40,54,55]. Before reaching the peak stress (σ_p), dislocation density and the degree of work hardening increase which results in nucleation of dislocation-free DRX-grains. With increasing flow stress up to its peak value, the rate of softening prevails over the work-hardening mechanism. Such phenomenon is common Ti-6Al-4V with low to medium stacking fault energy [54,55]. In general, flow stress characteristic depends on the critical strain, strain rate, and temperature. Thus, it is important to determine ε_c for the onset of DRX for different strain rate conditions.

The DRX mechanism contains recrystallization and grain growth kinetics which includes the peak strain (ε_p) and the DRX volume fraction (R_{DRX}) equation [40,41]. In the current work, the Johnson-Mehl-Avrami-Kolmogorov (JMAK) the model has been utilized to quantify the kinetics of DRX for peak stress and the dynamic recrystallization evolution that can be expressed as [40,55]:

$$R_{DRX} = 1 - exp\left[-\beta_d \left(\frac{\varepsilon - \varepsilon_c}{\varepsilon_{0.5}}\right)^{k_d}\right] \tag{7}$$

where β_d, k_d are the material constants; ε is the accumulated plastic strain ; ε_c is the critical strain for initiation of DRX, and $\varepsilon_{0.5}$ is the strain corresponding to 50% DRX. For Ti-6Al-4V, the values β_d and k_d can be considered as $\beta_d = 0.693$ and $k_d = 1.502$ [54].

In the present work, a hyperbolic tangent function has been employed to estimate the flow stress up to the peak stress of the stress–strain curves under hot deformation conditions [56,57]. The proposed flow stress model has been utilized to determine ε_c at the onset of DRX for different strain rate conditions which can be expressed as [57]:

$$\sigma = \sigma_i + (\sigma_p - \sigma_i)\left[\tanh\left(2\zeta\frac{\varepsilon}{\varepsilon_p}\right)\right]^{\varphi} \tag{8}$$

where σ_i and σ_p are the initial and peak stress values, respectively; ε_p is the peak strain; ζ and φ are the additional parameters that depend on strain rate and temperature. In order to obtain ζ and φ, following relationship have been utilized [57]:

$$\tanh^{-1}\left(\frac{\sigma-\sigma_i}{\sigma_p-\sigma_i}\right)^{1/\varphi} = 2\zeta\frac{\varepsilon}{\varepsilon_p}; \quad \ln\left(\frac{\sigma-\sigma_i}{\sigma_p-\sigma_i}\right) = \varphi\,\ln\left[\tanh\left(2\zeta\frac{\varepsilon}{\varepsilon_p}\right)\right] \tag{9}$$

where the parameters ζ and φ can be obtained from the slopes of the linear fitted $\tanh^{-1}\left(\frac{\sigma-\sigma_i}{\sigma_p-\sigma_i}\right)^{1/\varphi}$ vs. $2\frac{\varepsilon}{\varepsilon_p}$ and $\ln\left(\frac{\sigma-\sigma_i}{\sigma_p-\sigma_i}\right)$ vs. $\ln\left[\tanh\left(2\zeta\frac{\varepsilon}{\varepsilon_p}\right)\right]$ curves, respectively. To determine ε_c, the slope of the stress–strain curve at constant strain rate and temperature corresponding to work hardening rate, i.e. $\theta = \frac{\partial\sigma}{\partial\varepsilon}$ has been considered that provides :

$$\theta = 2\zeta\varphi\frac{\sigma_p-\sigma_i}{\varepsilon_p}\tanh\left(2\zeta\frac{\varepsilon}{\varepsilon_p}\right)^{\varphi-1}\left(1-\tanh\left(2\zeta\frac{\varepsilon}{\varepsilon_p}\right)^2\right) \tag{10}$$

Finally, ε_c can be expressed in terms of ε_p, ζ, and φ as follows :

$$\varepsilon_c = \frac{\varepsilon_p}{\zeta}\tanh^{-1}\left(\sqrt{\frac{1-\varphi}{1+\varphi}}\right) \tag{11}$$

In the CP-DRX framework, the DRX and CP models are linked through ε_c and R_{DRX}. During simulation, when the DRX volume fraction is less than R_{DRX}, all elements with $\varepsilon > \varepsilon_c$ have been identified as DRX-grains. Note, for simplicity, the crystallographic orientation of the DRX grains has not been taken into consideration. This is based on the experimentally observed fact that the DRX grain retains the same orientation as the parent grain [11,12]. The yield stress of the recrystallized grain $\sigma_Y^R = k\,\sigma_Y$; $\forall k < 1$ has been considered to be fixed on the onset of the DRX where $k(\partial\varepsilon/\partial t, \theta)$ is the additional parameter that can be calibrated from the softening characteristic of experimental flow stress–strain response. In order to obtain ε_c (i.e, from Eq. (11)) for different strain rate conditions, the values of ε_p, ζ, and φ have been calculated from experimental flow stress–strain curves. Subsequently,

Table 3
Calibrated kinetic parameters of DRX for Ti-6Al-4V at 800 °C for different strain-rate conditions.

$\partial\varepsilon/\partial t$ (s^{-1})	ε_f	$\%\, R_{DRX}$	β_c	k_d	ζ	φ	ε_c	$\varepsilon_{0.5}$
0.001	0.50	37.10	0.693	1.502	44.42	1.72	0.1037	0.9123
0.1	0.80	14.4	0.693	1.502	30.52	1.67	0.1274	1.7645

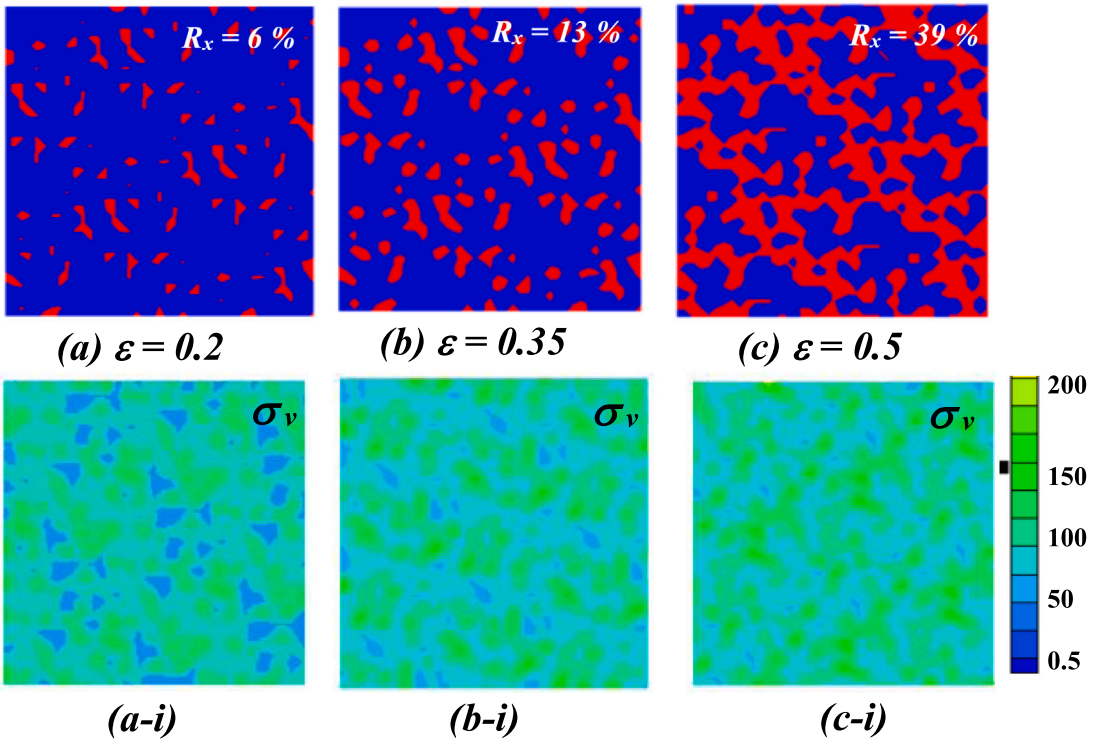

Fig. 4. Evolution of DRX grains (in red) inside the uncrystallized grain matrix (in blue) with randomly assigned crystal orientation in initial representative 2D grain structure for (a) $\varepsilon = 0.2$, (b) $\varepsilon = 0.35$, and (c) $\varepsilon = 0.5$ where R_x represents the volume fraction of recrystallized grains; (a–i)–(c–i) corresponding distribution of average von Mises stress (σ_v) for strain rate $\partial\varepsilon/\partial t = 0.001\ s^{-1}$. All stress values are in MPa. (For interpretation of the references to color in this figure legend, the reader is referred to the web version of this article.)

$\varepsilon_{0.5}$ has been obtained from Eq. (7) with know values of β_d, k_d, and ε_c for different strain rate conditions where the value of R_{DRX} has been measured directly from the experiment. All the kinetics parameters associated with the DRX for the different strain rates have been outlined in Table 3. In the future, the parameters β_d, k_d can be calibrated directly from the experiments to establish a robust integration of DRX kinetics into the CP-DRX model.

6. Results and discussions

To study the influence of different strain rates on the evolution of DRX grain morphology and texture in Ti-6Al-4V, in the present study, two different strain rates $\partial\varepsilon/\partial t = 0.001\ s^{-1}$ and $\partial\varepsilon/\partial t = 0.1\ s^{-1}$ have been considered corresponding to final strain $\varepsilon_f = 0.5$ and $\varepsilon_f = 0.8$, respectively at elevated constant temperature; $T = 800$ °C. The plastic stress–strain response obtained from the simulation results has been directly compared with experimental observations to evaluate to what extent the proposed two-phase CP-DRX framework can predict the flow stress–strain characteristics focusing on the softening behavior during DRX.

6.1. Simulation for calibrating optimum slip system parameters

In order to calibrate optimum slip system parameters for both α-Ti and β-Ti, an initial representative 2D grain structure has been considered as 60 × 60 grid with 3600 grains where each grain is associated with random grain orientation. The initial phase fraction of α-Ti and β-Ti phases in the parent material have been determined from the experiential phase map with volume fraction of 95% HCP α-Ti and 5% BCC β-Ti as shown in Fig. 1-(a). In the initial representative grain structure, these two phases have been randomly assigned for the calibration of optimum slip system parameters as shown in Fig. 4-(a). Assuming plane strain condition, a homogeneous compressive strain has been applied on the top edge with a constant strain rate until the prescribed final strain has been achieved. For the strain rate, $\partial\varepsilon/\partial t = 0.001\ s^{-1}$, the evolution of recrystallized grains (red) inside the unrecrystallized matrix (blue) during various intermediate strains has been presented in Fig. 4(a)–(c). The recrystallized grains appear when the local strain value exceeds a critical strain, i.e., $\varepsilon > \varepsilon_c$ during the deformation process. Depending on the strain distribution, recrystallized grains emerge, grow, and finally coalesce. The corresponding distribution of average von Mises stresses σ_v for intermediate strain values has been shown in Fig. 4 (a-i)–(c-i). The comparison of (0001) and $(10\bar{1}0)$ pole Figures at $\varepsilon_f = 0.8$ between CP-DRX simulation and experiment has been depicted in Fig. 5-(a). The pole figures have been plotted using MATLAB toolbox MTEX [58]. Even for initial random texture distribution in the representative 2D grain structure, the CP-DRX simulation predicts the final texture evolution reasonably well. Finally, the CP-DRX stress–strain curves for different strain-rate conditions obtained during calibration of optimum slip system parameters for both α-Ti and β-Ti through experimental compression stress–strain data have been shown in Fig. 5-(b, c).

6.2. Experimentally informed microstructural representation

As mentioned earlier, in the proposed CP-DRX framework, α and β-Ti phases have been modeled explicitly. Thus, it is important to

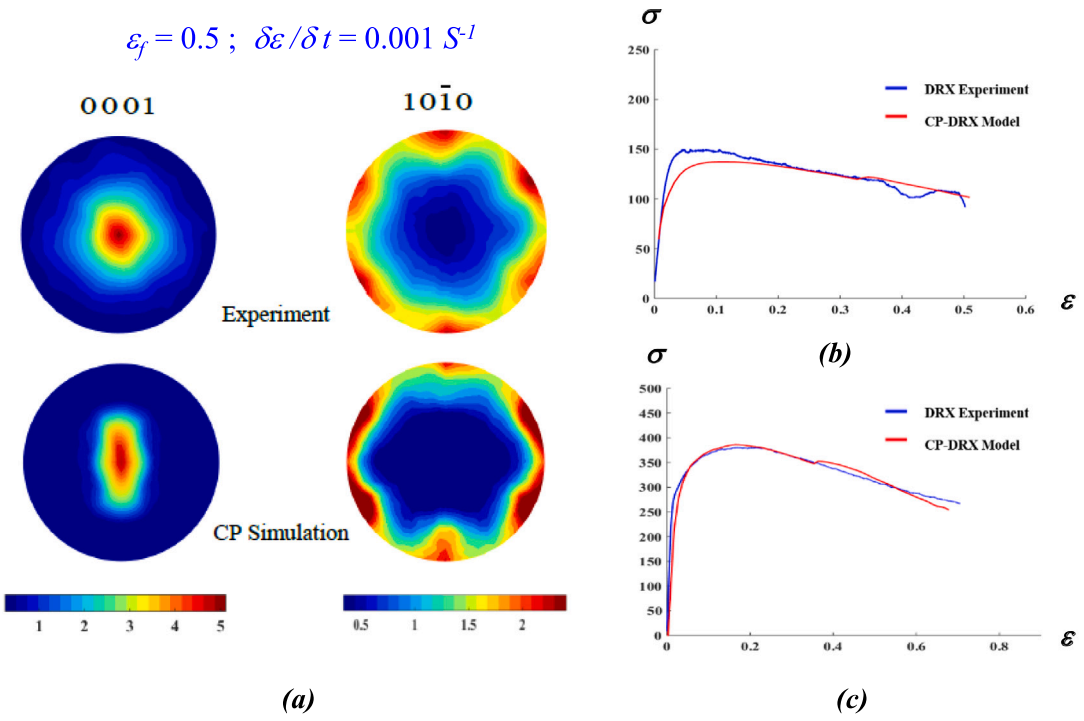

Fig. 5. Comparison of (a) (0001) and (10$\bar{1}$0) pole figures at final compressive strain $\varepsilon_f = 0.5$ for $\partial\varepsilon/\partial t = 0.001\ s^{-1}$; (b, c) stress–strain curves at $\partial\varepsilon/\partial t = 0.001\ s^{-1}$ and $\partial\varepsilon/\partial t = 0.1\ s^{-1}$ between experiment and CP-DRX prediction considering the optimum design of slip system parameters for randomly assigned crystal orientation in the initial representative 2D grain structure of Ti-6Al-4V as shown in Fig. 4. All stress values are in MPa.

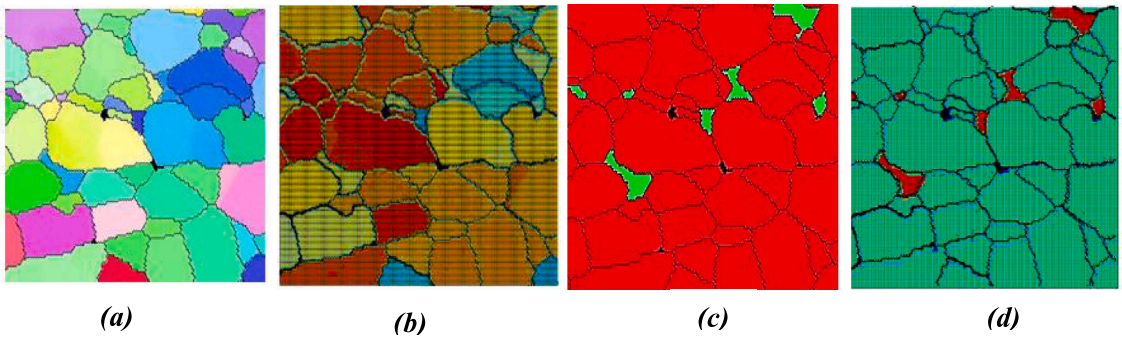

Fig. 6. (a, c) Representative experimental EBSD and IPF image showing phase fraction of 95% HCP β-Ti (red) and 5% BCC α-Ti (green) in parent Ti-6Al-4V sample at ambient temperature; (b, d) corresponding morphologically representative microstructural finite element mesh used to simulate CP-DRX model. (For interpretation of the references to color in this figure legend, the reader is referred to the web version of this article.)

distinguish these two phases in the finite element microstructural mesh. To this end, EBSD and IPF information have been combined in the CP-DRX framework to capture the exact grain morphology and location of α and β-Ti phases to incorporate a realistic experimentally informed microstructural representation. In the model, a morphologically representative microstructural finite element mesh selected from the EBSD image containing a total of 62 grains has been considered as shown in Fig. 6-(a). To characterize the grain shapes and crystallographic orientations of the two phases, an in-house MATLAB image processing algorithm has been developed which can accurately reproduce grain morphology with finite element mesh and identify phase information from the inputted EBSD and IPF images. The finite element mesh corresponding to each grain has been assigned to a unique grain identifier to distinguish between different grains. Additionally, a phase identifier has been embedded in each grain according to the IPF image information. After the spatial assignment of the finite element mesh for each grain, information on crystallographic orientations from the EBSD data has been incorporated. The orientation of each grain has been calculated by averaging all the EBSD data points within the grain and supplemented into the CP-DRX model. The initial phase fraction of α and β phase in parent material has been determined from IPF as shown in Fig. 1-(a). The present study considers initial 95% HCP β-Ti and 5% BCC α-Ti for all CP-DRX simulations. To represent the grain morphology of the inputted microstructure accurately, a rectangular finite element mesh with a finer grid of 160 × 160 consisting of 25600 elements has been considered. As shown in Fig. 6-(c), an initial experimental IPF image consisting of phase fraction of 95% HCP β-Ti (red) and 5% BCC α-Ti (green) in parent Ti-6Al-4V sample has been inputted to the CP-DRX model. Corresponding finite element mesh representation containing HCP β-Ti (red) and BCC α-Ti (green) as been shown in Fig. 6-(d) which indicates that the EBSD image processing algorithm can reproduce the experimental grain morphology accurately. The sample is compressed on the top surface and restrained on the bottom surface. The present study focuses on evaluating the average strain on the surface of the Ti-6Al-4V sample incorporating morphologically representative mesh. The effect of both strain rates and

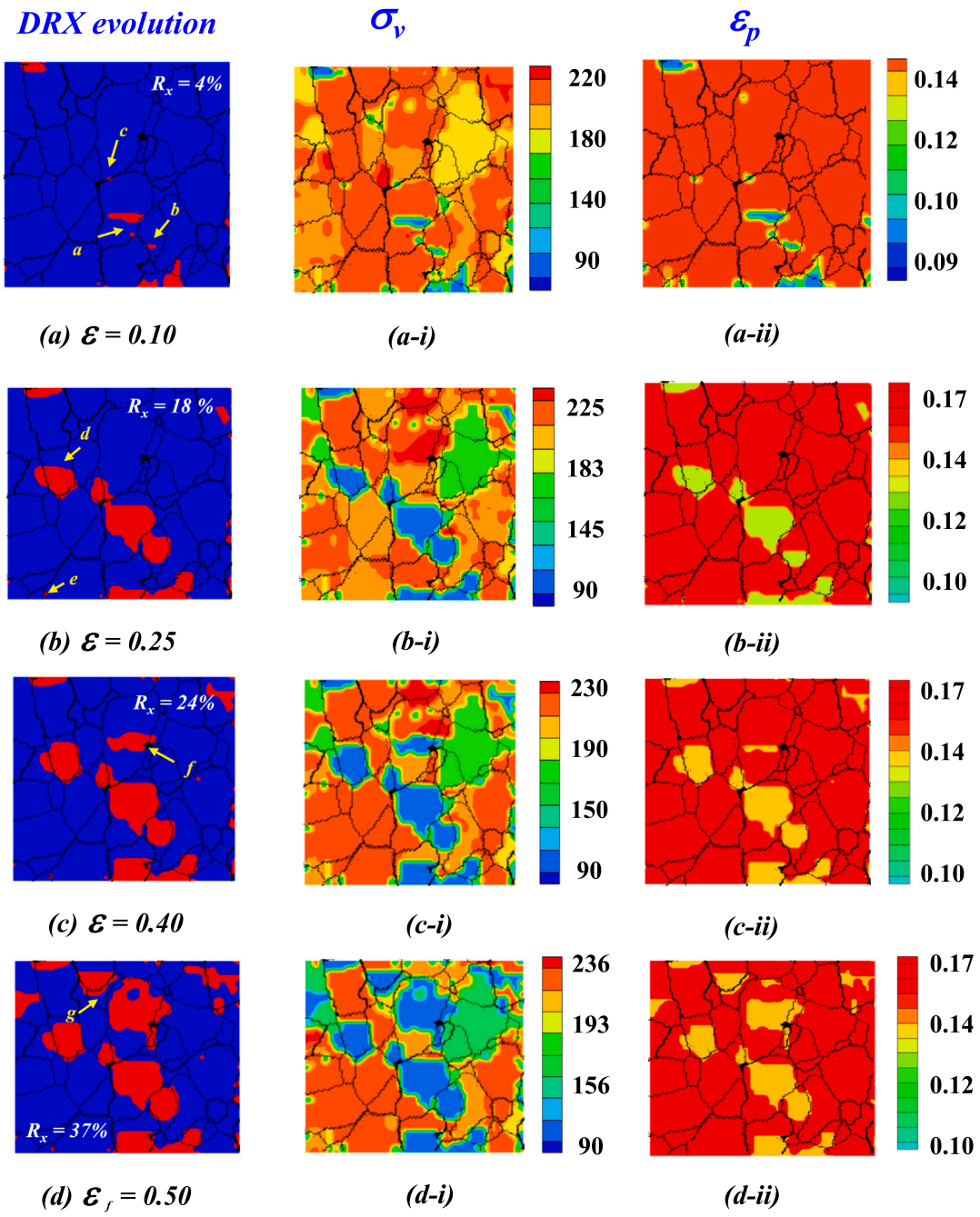

Fig. 7. Left column: Evolution of DRX-grain at different strain where R_x represents the volume fraction of recrystallized grains, second and third columns: corresponding average Von Mises stress σ_v and plastic strain ε_p for low strain rate $\partial\varepsilon/\partial t = 0.001\ s^{-1}$ in the representative microstructure of Ti-6Al-4V. The blue and red regions represent non-DRX and DRX-grain, respectively. All the values of stress are in MPa.

final strain on the DRX microstructural evolution, texture formation, and stress–strain response have been explored which has been detailed in the subsequent sections.

6.3. Results for different strain rate conditions

6.3.1. Evolution of DRX for low strain rate

This section reports the evolution of DRX in the representative EBSD microstructure of parent Ti-6Al-4V sample for relatively low strain rate condition $\partial\varepsilon/\partial t = 0.001\ s^{-1}$ as shown in Fig. 7. Additionally, the distribution of average von Mises stresses σ_v and plastic strain ε_p have been plotted for different intermediate strains. At strain $\varepsilon = 0.1$, new DRX-grains (i.e., grains-*a*, *b*, *c*) have been nucleated predominately in the grain boundary and triple grain boundaries as shown in Fig. 7-(a). This is due to texture miss-orientation at grain boundary leading to large strain accumulation which exceeds the critical strain and therefore facilitates the formation of DRX-grains. Moreover, due to the relatively large strain concentration on the edge of the sample, several DRX grains have been formed surrounding the top and bottom edges of the microstructural sample. With increasing strain $\varepsilon = 0.25$, the appearance of additional DRX-grains (i.e., grains-*d*, *e*) has been observed in the other grain boundaries as well as in the sub-grains as shown in Fig. 7-(b). The portions of sub-grain correspond to relatively low σ_v are DRX-grains indicating stress-relaxing during the DRX process. With increasing ε, both σ_v and ε_p increase nearby DRX-grains as well as grain boundaries. With the further accumulation of ε_p, such regions became the nucleation spots for new DRX-grains. Previously formed DRX grains

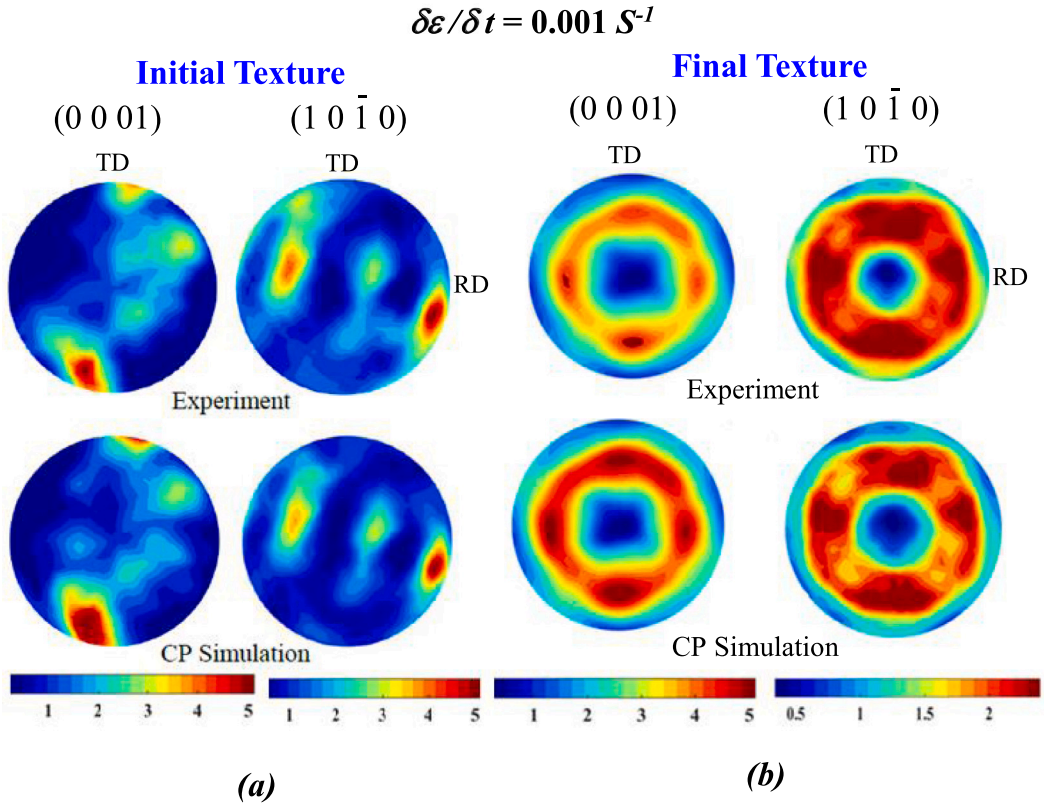

Fig. 8. Comparison of (0001) and (10$\bar{1}$0) pole figures for (a) initial texture in parent Ti-6Al-4V sample at ambient temperature; (b) texture at final compressive strain $\varepsilon_f = 0.5$ for strain rate $\partial\varepsilon/\partial t = 0.001\ s^{-1}$ between experimental EBSD microstructure in Fig. 6-(a) and CP-DRX simulation in Fig. 6-(b).

tend to extend inside the sub-grains, and finally coalesce with newly formed DRX grains. The stress and strain distribution indicate that the unrecrystallized grains attend significantly high σ_v and ε_p compared to DRX-grains. With further increase of $\varepsilon = 0.40$, new-DRX grains tend to form in the grain boundaries and extend to the sub-grains (see grain-f) as marked in Fig. 7-(c). At final strain $\varepsilon_f = 0.50$, the formation of some additional DRX-grains (for example, grain-g) takes place and coalesces with previously recrystallized grains. It is noteworthy to mention that at final strain, previously formed DRX-grains became stationary and the degree of recrystallization increases predominantly due to relatively new DRX-grains as illustrated in Fig. 7-(d). The volume fraction of recrystallized grains R_x has been calculated during the deformation process. For $\partial\varepsilon/\partial t = 0.001\ s^{-1}$, the final R_x was found to be $R_x = 39.72\%$, which is in good agreement with experimental data in Table 3.

6.3.2. Pole figures comparison for low strain rate condition

The pole figures obtained from the experimental EBSD microstructure and CP-DRX simulation have been compared for relatively low strain rate $\partial\varepsilon/\partial t = 0.001\ s^{-1}$ as shown in Fig. 8. The (0001) and (10$\bar{1}$0) pole figures obtained from the parent experimental EBSD texture is well reproduced by the CP-DRX model by accurately accounting for initial grain morphology and orientation for undeformed microstructure as shown in Fig. 8-(a). It indicates the correctness and proper distribution of grain texture in the proposed experimentally-informed microstructural mesh for CP-DRX simulation. As shown in Fig. 8-(b), the pole figures of the deformed sample are plotted at final strain $\varepsilon_f = 0.50$ which indicates that the simulated pole figures capture the expected features of the microstructural sample during the hot-compression process. Under compression, the $\langle c \rangle$ axis moves to the ND poles along normal to the ND direction. Both experimental and CP-DRX results realign the $\langle c \rangle$ axis in the compression direction indicating a strong basal texture. The primary mechanism of such texture distribution can be due to softening of the recrystallized grain due to high temperature.

6.3.3. Evolution of DRX for high strain rate

For relatively high strain rate $\partial\varepsilon/\partial t = 0.1\ s^{-1}$, the evolution of DRX grain, distribution of σ_v, and ε_p are shown in Fig. 9. For strain $\varepsilon = 0.1$, newly DRX grains are predominantly nucleated in the grain boundaries of the representative microstructure. For example, grains-a, b in Fig. 9-(a) nucleate at the triple grain boundaries which are energetically most favorable for the appearance of new DRX-grains. Corresponding Von-Mises stress and plastic strain are relatively low in these grains and high outside the DRX-grain region indicating stress and strain relaxation during DRX as shown in Figs. 9 (a-i)–(a-ii). With increasing strain $\varepsilon = 0.35$ and $\varepsilon = 0.65$, newly DRX grains appear, and pre-existing DRX grains start to grow in the sub-grain region. The plastic strain relaxes while the DRX grain grows inside the grain and it accumulates outside the DRX region which further serves as nucleation spots for new DRX grains. At final strain $\varepsilon_f = 0.80$, DRX grains continue to grow and start to coalesce with neighborhood DRX grains with increasing ε_p the σ_v increases nearby DRX grains. At this point, there are no additional nucleation sites for newly DRX grains have been noticed.

6.3.4. Pole figures comparison for high strain rate condition

The pole figures obtained from the experimental EBSD microstructure and CP-DRX simulation have been compared for $\partial\varepsilon/\partial t = 0.1\ s^{-1}$. The comparison of (0001) and (10$\bar{1}$0) pole figures between the initial texture and texture after final strain $\varepsilon_f = 0.80$ has been depicted in Fig. 10. From the result, one can see the initial feature of EBSD texture has been well reproduced by the CP-DRX model by accurately accounting for initial grain morphology and orientation as shown in Fig. 10-(a). At final strain $\varepsilon_f = 0.80$, CP-DRX The results show that the simulated pole figures capture the expected features of the simulated sample by correctly identifying compression poles during high strain rate compression at elevated temperature as depicted in Fig. 10-(b).

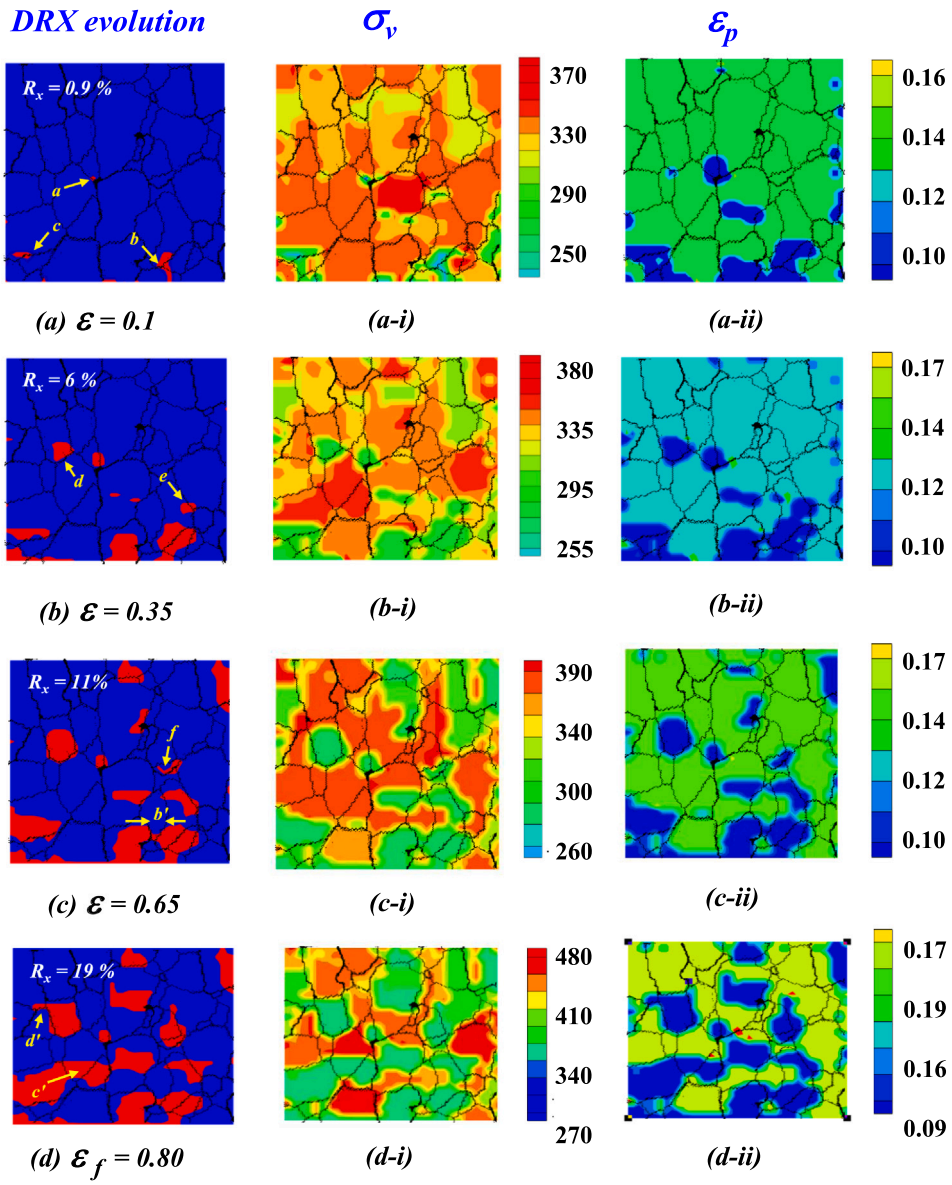

Fig. 9. Left column: Evolution of DRX-grain at different strain where R_x represents the volume fraction of recrystallized grains, Second and third columns: corresponding average Von Mises stress σ_v and plastic strain ε_p for high strain rate $\partial\varepsilon/\partial t = 0.1\ s^{-1}$ in the representative microstructure of Ti-6Al-4V. The blue and red regions represent non-DRX and DRX-grain, respectively. All the values of stress are in MPa. (For interpretation of the references to color in this figure legend, the reader is referred to the web version of this article.)

6.4. Comparison of flow stress–strain curves for different strain rates

In this section, the effect of different strain rates on the flow stress–strain response in Ti-6Al-4V during the DRX process has been discussed. As shown in Fig. 11, the predicted flow stress–strain response from CP-DRX model has been directly compared with DRX experimental results for two different strain rate conditions $\partial\varepsilon/\partial t = 0.001\ s^{-1}$ and $\partial\varepsilon/\partial t = 0.1\ s^{-1}$ at temperature $T = 800\ °C$. Experimental results indicate initial rapid strain hardening for both strain rates. With a higher strain rate, flow stress increases. For relatively low $\partial\varepsilon/\partial t = 0.001\ s^{-1}$, there exist multiple peaks in the stress–strain profile after the post-work hardening phase, in particular, $0.085 \leqslant \varepsilon \leqslant 0.18$ as shown in Fig. 11-(a). On the contrary, there is single peak stress at relatively high $\partial\varepsilon/\partial t = 0.1\ s^{-1}$ as depicted in Fig. 11-(b). For both strain rate, softening characteristic has been observed during the DRX process. During this region, flow stress monotonically decreases with increasing plastic strain. The slope of the flow stress–strain curve negatively increases with increasing strain rate. It is noteworthy to mention that there exist stress oscillation in experimental observation for $\partial\varepsilon/\partial t = 0.001\ s^{-1}$ in the region $0.35 \leqslant \varepsilon \leqslant 0.5$ indicating occurrence of several recrystallization and grain growth cycles before reaching the steady state of failure. These unique features of mechanical responses are well reproduced by the proposed CP-DRX model. Qualitatively, both experimental and CP-DRX results for true stress–strain curves reveal that at a given strain rate, the flow stress decreases with increasing final strain associated with a decrease in the degree of softening. Quantitatively, the CP-DRX stress–strain prediction is in good agreement with experimental yield stress as well as non-linear softening characteristic for the case of relatively low $\partial\varepsilon/\partial t = 0.001\ s^{-1}$. For relatively high $\partial\varepsilon/\partial t = 0.1\ s^{-1}$, the CP-DRX model prediction underestimates the softening pattern observed in the experiment flow stress–strain response. This difference may be attributed to adiabatic heating [59], dynamic recovery [5], creep [60], and additional mechanisms during the experimental deformation process. It is noteworthy to mention that the stress oscillation in CP-DRX flow stress prediction as shown in Fig. 11-(a) indicates the occurrence of several recrystallization and grain growth cycles before reaching the

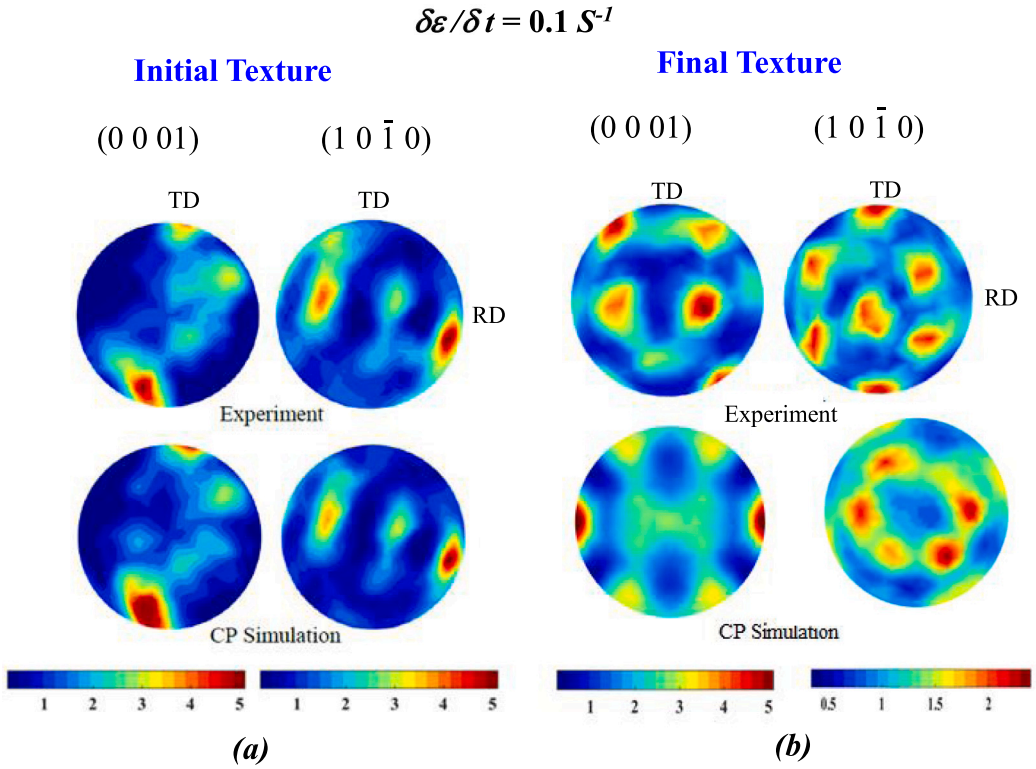

Fig. 10. Comparison of (0001) and (10$\bar{1}$0) pole figures for (a) initial texture in parent Ti-6Al-4V sample at ambient temperature; (b) texture at final compressive strain $\varepsilon_f = 0.5$ for strain rate $\partial\varepsilon/\partial t = 0.001\ s^{-1}$ between experimental EBSD microstructure in Fig. 6-(a) and CP-DRX simulation in Fig. 6-(b).

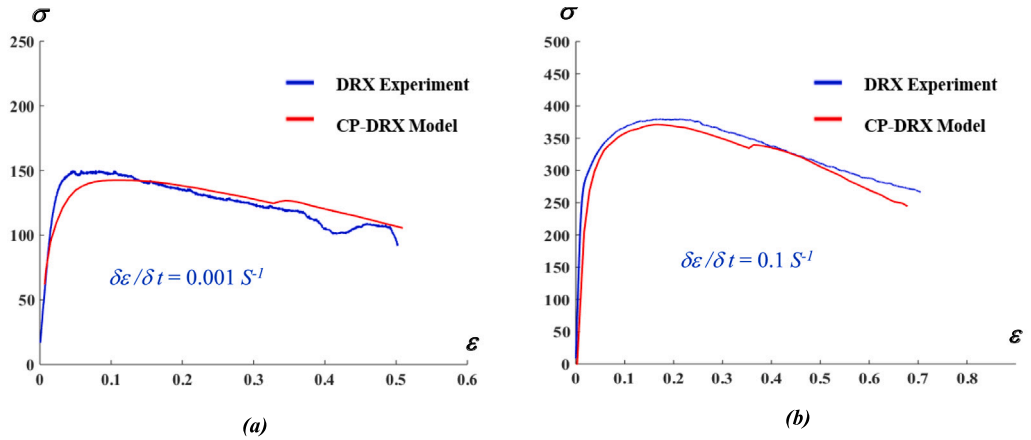

Fig. 11. Comparison of flow stress–strain response during deformation of Ti-6Al-4V sample between DRX experimental result and CP-DRX model for constant strain rate (a) $\partial\varepsilon/\partial t = 0.001\ s^{-1}$ with $\varepsilon_f = 0.5$; (b) $\partial\varepsilon/\partial t = 0.1\ s^{-1}$ at temperature $T = 800$ °C.

steady state. Such stress behavior before reaching the steady state may depend on the initial grain size, temperature, and strain rate condition. Additionally, the flow stress increases with the increasing strain rate while the degree of nonlinearity in the softening behavior decreases. From the aforementioned comparison of the flow stress–strain character, it can be concluded that the softening effect is pronounced at the lower strain rate as well as higher final strain. For the lower strain rate, the prediction of the CP model captures experimental flow softening behavior significantly well.

The current research demonstrates the effectiveness of the proposed CP-DRX model to reproduce experimental softening behavior observed during DRX in Ti-6Al-4V. The model can correctly predict the DRX volume fraction during microstructure evolutions as well as crystal orientation during thermo-mechanical processing. However, the current model can only predict two different strain rate conditions Thus, the predictive power of the CP-DRX needs to be extended for a relatively large range of strain rate conditions. Nevertheless, the proposed modeling approach can be extended to capture the DRX phenomenon during cycling loading. Future studies will focus on implementing grain boundary formulation in the CP model. Additionally, various phase-field (PF) approaches [61–65] can be integrated into the CP-DRX model to capture phase transformation during thermo-mechanical loading. The prediction capability on the flow stress behavior and texture evolution can be further enhanced by incorporating data-driven physics-informed neural networks (PINNs)-based constitutive modeling approaches [66–69].

7. Conclusion

Summarizing, in this paper, a two-phase crystal plasticity finite element model has been developed with accounted for the kinetics of DRX and combined with experimental characterization to make a computationally efficient Integrated Computational Materials Engineering (ICME) framework. The slip system parameters, as well as elastic properties from both α and β phases of Ti, are calibrated for elevated temperature and different strain rates for Ti-6Al-4V alloys to predict the flow stress–strain behavior of DRX during the deformation process. The evolution of dynamically recrystallized grains volume fraction and stress–strain behavior for different strain rates are discussed and directly compared with experiments. The model can capture the softening in experimental stress–strain behavior occurring due to DRX and predict the recrystallization texture.

CRediT authorship contribution statement

Arunabha M. Roy: Conceptualization, Data curation, Formal analysis, Investigation, Methodology, Software, Validation, Visualization, Writing – original draft. **Raymundo Arróyave:** Formal analysis, Investigation, Writing – review & editing, Supervision, Funding. **Veera Sundararaghavan:** Conceptualization, Formal analysis, Investigation, Writing – review & editing, Supervision, Funding.

Declaration of competing interest

The authors declare that they have no known competing financial interests or personal relationships that could have appeared to influence the work reported in this paper.

Data availability

Data will be made available on request.

Acknowledgments

We acknowledge the support of the Lightweight Innovation for Tomorrow (LIFT) program which funded this work. The authors are grateful to Dr. John Allison and Dr. Riddhiman Bhattacharya from the University of Michigan, Ann Arbor for their kind guidance and assistance. The experimental data presented in this paper was collected and analyzed by Dr. R. Bhattacharya during his postdoctoral research. The computations have been carried out as part of research supported by the U.S. Department of Energy, Office of Basic Energy Sciences, Division of Materials Sciences and Engineering under Award no. DE-SC0008637 funds the Predictive Integrated Structural Materials Science (PRISMS) Center at the University of Michigan. RA acknowledges the support of National Science Foundation (NSF) through Grant No. 2119103.

References

[1] A. Majorell, S. Srivatsa, R. Picu, Mechanical behavior of Ti-6Al-4V at high and moderate temperatures—Part I: Experimental results, Mater. Sci. Eng. A 326 (2) (2002) 297–305.
[2] M. Zhang, J. Zhang, D. McDowell, Microstructure-based crystal plasticity modeling of cyclic deformation of Ti-6Al-4V, Int. J. Plast. 23 (8) (2007) 1328–1348.
[3] X. Fan, H. Yang, Internal-state-variable based self-consistent constitutive modeling for hot working of two-phase titanium alloys coupling microstructure evolution, Int. J. Plast. 27 (11) (2011) 1833–1852.
[4] F.J. Humphreys, M. Hatherly, Recrystallization and Related Annealing Phenomena, Elsevier, 2012.
[5] K. Huang, R. Logé, A review of dynamic recrystallization phenomena in metallic materials, Mater. Des. 111 (2016) 548–574.
[6] A.S. Khan, R. Kazmi, B. Farrokh, Multiaxial and non-proportional loading responses, anisotropy and modeling of Ti-6Al-4V titanium alloy over wide ranges of strain rates and temperatures, Int. J. Plast. 23 (6) (2007) 931–950.
[7] J.H. Sung, J.H. Kim, R. Wagoner, A plastic constitutive equation incorporating strain, strain-rate, and temperature, Int. J. Plast. 26 (12) (2010) 1746–1771.
[8] L. Huang, L. Geng, A. Li, X. Cui, H. Li, G. Wang, Characteristics of hot compression behavior of Ti–6.5 Al–3.5 Mo–1.5 Zr–0.3 Si alloy with an equiaxed microstructure, Mater. Sci. Eng. A 505 (1–2) (2009) 136–143.
[9] Y. Zong, D. Shan, M. Xu, Y. Lv, Flow softening and microstructural evolution of TC11 titanium alloy during hot deformation, J. Mater Process. Technol. 209 (4) (2009) 1988–1994.
[10] B. Poorganji, M. Yamaguchi, Y. Itsumi, K. Matsumoto, T. Tanaka, Y. Asa, G. Miyamoto, T. Furuhara, Microstructure evolution during deformation of a near-α titanium alloy with different initial structures in the two-phase region, Scr. Mater. 61 (4) (2009) 419–422.
[11] R. Ding, Z. Guo, Microstructural evolution of a Ti-6Al-4V alloy during β-phase processing: experimental and simulative investigations, Mater. Sci. Eng. A 365 (1–2) (2004) 172–179.
[12] P. Vo, M. Jahazi, S. Yue, P. Bocher, Flow stress prediction during hot working of near-α titanium alloys, Mater. Sci. Eng. A 447 (1–2) (2007) 99–110.
[13] R. Ding, Z. Guo, Coupled quantitative simulation of microstructural evolution and plastic flow during dynamic recrystallization, Acta Mater. 49 (16) (2001) 3163–3175.
[14] T. Sakai, A. Belyakov, R. Kaibyshev, H. Miura, J.J. Jonas, Dynamic and post-dynamic recrystallization under hot, cold and severe plastic deformation conditions, Prog. Mater. Sci. 60 (2014) 130–207.
[15] F. Qin, H. Zhu, Z. Wang, X. Zhao, W. He, H. Chen, Dislocation and twinning mechanisms for dynamic recrystallization of as-cast Mn18Cr18N steel, Mater. Sci. Eng. A 684 (2017) 634–644.
[16] L. Huang, F. Qi, P. Hua, L. Yu, F. Liu, W. Sun, Z. Hu, Discontinuous dynamic recrystallization of inconel 718 superalloy during the superplastic deformation, Metall. Mater. Trans. A 46 (9) (2015) 4276–4285.
[17] A.R. McAndrew, P.A. Colegrove, C. Bühr, B.C. Flipo, A. Vairis, A literature review of Ti-6Al-4V linear friction welding, Prog. Mater. Sci. 92 (2018) 225–257.
[18] E. Dalgaard, P. Wanjara, J. Gholipour, X. Cao, J. Jonas, Linear friction welding of a near-β titanium alloy, Acta Mater. 60 (2) (2012) 770–780.
[19] F. Schroeder, R. Ward, A. Walpole, R. Turner, M. Attallah, J.-C. Gebelin, R. Reed, Linear friction welding of Ti6Al4V: experiments and modelling, Mater. Sci. Technol. 31 (3) (2015) 372–384.
[20] A. Arsenlis, D.M. Parks, Modeling the evolution of crystallographic dislocation density in crystal plasticity, J. Mech. Phys. Solids 50 (9) (2002) 1979–2009.
[21] K.-S. Cheong, E.P. Busso, Discrete dislocation density modelling of single phase FCC polycrystal aggregates, Acta Mater. 52 (19) (2004) 5665–5675.
[22] A. Ma, F. Roters, D. Raabe, A dislocation density based constitutive model for crystal plasticity FEM including geometrically necessary dislocations, Acta Mater. 54 (8) (2006) 2169–2179.
[23] I. Beyerlein, C. Tomé, A dislocation-based constitutive law for pure Zr including temperature effects, Int. J. Plast. 24 (5) (2008) 867–895.
[24] V. Hasija, S. Ghosh, M.J. Mills, D.S. Joseph, Deformation and creep modeling in polycrystalline Ti–6Al alloys, Acta Mater. 51 (15) (2003) 4533–4549.
[25] Z. Zheng, D.S. Balint, F.P. Dunne, Dwell fatigue in two Ti alloys: an integrated crystal plasticity and discrete dislocation study, J. Mech. Phys. Solids 96 (2016) 411–427.
[26] Z. Zhang, T.-S. Jun, T.B. Britton, F.P. Dunne, Determination of Ti-6242 α and β slip properties using micro-pillar test and computational crystal plasticity, J. Mech. Phys. Solids 95 (2016) 393–410.
[27] T. Ozturk, A.D. Rollett, Effect of microstructure on the elasto-viscoplastic deformation of dual phase titanium structures, Comput. Mech. 61 (1) (2018) 55–70.
[28] H. Li, C. Wu, H. Yang, Crystal plasticity modeling of the dynamic recrystallization of two-phase titanium alloys during isothermal processing, Int. J. Plast. (51) (2013) 271–291.
[29] J.A. Moore, N.R. Barton, J. Florando, R. Mulay, M. Kumar, Crystal plasticity modeling of β phase deformation in Ti-6Al-4V, Modelling Simul. Mater. Sci. Eng. 25 (7) (2017) 075007.
[30] Z. Zhang, F.P. Dunne, Microstructural heterogeneity in rate-dependent plasticity of multiphase titanium alloys, J. Mech. Phys. Solids 103 (2017) 199–220.
[31] K. Kapoor, Y.S.J. Yoo, T.A. Book, J.P. Kacher, M.D. Sangid, Incorporating grain-level residual stresses and validating a crystal plasticity model of a two-phase Ti-6Al-4 V alloy produced via additive manufacturing, J. Mech. Phys. Solids 121 (2018) 447–462.
[32] Z. Zheng, S. Waheed, D.S. Balint, F.P. Dunne, Slip transfer across phase boundaries in dual phase titanium alloys and the effect on strain rate sensitivity, Int. J. Plast. 104 (2018) 23–38.
[33] X. Wang, J. Li, F. Cazes, G. Dirras, A three-dimensional microstructure-based crystal plasticity model for coarse-grained and harmonic-structured Ti-6Al-4V under monotonic and cyclic shear loading, Acta Mech. 231 (12) (2020) 4991–5005.
[34] K. Kapoor, P. Ravi, R. Noraas, J.-S. Park, V. Venkatesh, M.D. Sangid, Modeling Ti-6Al-4V using crystal plasticity, calibrated with multi-scale experiments, to understand the effect of the orientation and morphology of the α and β phases on time dependent cyclic loading, J. Mech. Phys. Solids 146 (2021) 104192.

[35] T.-L. Cheng, Y.-H. Wen, J.A. Hawk, Diffuse interface approach to modeling crystal plasticity with accommodation of grain boundary sliding, Int. J. Plast. 114 (2019) 106–125.
[36] A. Ask, S. Forest, B. Appolaire, K. Ammar, O.U. Salman, A cosserat crystal plasticity and phase field theory for grain boundary migration, J. Mech. Phys. Solids 115 (2018) 167–194.
[37] Y. Li, S. Hu, E. Barker, N. Overman, S. Whalen, S. Mathaudhu, Effect of grain structure and strain rate on dynamic recrystallization and deformation behavior: A phase field-crystal plasticity model, Comput. Mater. Sci. 180 (2020) 109707.
[38] J. Allison, D. Backman, L. Christodoulou, Integrated computational materials engineering: a new paradigm for the global materials profession, Jom 58 (11) (2006) 25–27.
[39] J.H. Panchal, S.R. Kalidindi, D.L. McDowell, Key computational modeling issues in integrated computational materials engineering, Comput. Aided Des. 45 (1) (2013) 4–25.
[40] P. Kalu, D. Waryoba, A JMAK-microhardness model for quantifying the kinetics of restoration mechanisms in inhomogeneous microstructure, Mater. Sci. Eng. A 464 (1–2) (2007) 68–75.
[41] J.J. Jonas, X. Quelennec, L. Jiang, É. Martin, The avrami kinetics of dynamic recrystallization, Acta Mater. 57 (9) (2009) 2748–2756.
[42] J. Allison, Integrated computational materials engineering: A perspective on progress and future steps, Jom 63 (4) (2011) 15.
[43] L. Anand, M. Kothari, A computational procedure for rate-independent crystal plasticity, J. Mech. Phys. Solids 44 (4) (1996) 525–558.
[44] M. Yaghoobi, S. Ganesan, S. Sundar, A. Lakshmanan, S. Rudraraju, J.E. Allison, V. Sundararaghavan, PRISMS-Plasticity: An open-source crystal plasticity finite element software, Comput. Mater. Sci. 169 (2019) 109078.
[45] A. Githens, S. Ganesan, Z. Chen, J. Allison, V. Sundararaghavan, S. Daly, Characterizing microscale deformation mechanisms and macroscopic tensile properties of a high strength magnesium rare-earth alloy: A combined experimental and crystal plasticity approach, Acta Mater. 186 (2020) 77–94.
[46] G. Lütjering, J.C. Williams, Titanium, Springer Science & Business Media, 2007.
[47] S. Balasubramanian, L. Anand, Plasticity of initially textured hexagonal polycrystals at high homologous temperatures: application to titanium, Acta Mater. 50 (1) (2002) 133–148.
[48] L. Nervo, A. King, A. Fitzner, W. Ludwig, M. Preuss, A study of deformation twinning in a titanium alloy by X-ray diffraction contrast tomography, Acta Mater. 105 (2016) 417–428.
[49] J. Williams, R. Baggerly, N. Paton, Deformation behavior of HCP Ti-Al alloy single crystals, Metall. Mater. Trans. A 33 (3) (2002) 837–850.
[50] P.R. Dawson, E.B. Marin, Computational mechanics for metal deformation processes using polycrystal plasticity, Adv. Appl. Mech. 34 (1997) 77–169.
[51] P. Acar, A. Ramazani, V. Sundararaghavan, Crystal plasticity modeling and experimental validation with an orientation distribution function for Ti-7Al alloy, Metals 7 (11) (2017) 459.
[52] H. Ledbetter, H. Ogi, S. Kai, S. Kim, M. Hirao, Elastic constants of body-centered-cubic titanium monocrystals, J. Appl. Phys. 95 (9) (2004) 4642–4644.
[53] H. Ogi, S. Kai, H. Ledbetter, R. Tarumi, M. Hirao, K. Takashima, Titanium's high-temperature elastic constants through the hcp–bcc phase transformation, Acta Mater. 52 (7) (2004) 2075–2080.
[54] J. Xiao, D. Li, X. Li, T. Deng, Constitutive modeling and microstructure change of Ti-6Al-4V during the hot tensile deformation, J. Alloys Compd. 541 (2012) 346–352.
[55] J. Liu, Z.-s. Cui, L.-q. Ruan, A new kinetics model of dynamic recrystallization for magnesium alloy AZ31B, Mater. Sci. Eng. A 529 (2011) 300–310.
[56] S. Solhjoo, Determination of flow stress under hot deformation conditions, Mater. Sci. Eng. A 552 (2012) 566–568.
[57] S. Solhjoo, A.I. Vakis, Y.T. Pei, Two phenomenological models to predict the single peak flow stress curves up to the peak during hot deformation, Mech. Mater. 105 (2017) 61–66.
[58] F. Bachmann, R. Hielscher, H. Schaeben, Texture analysis with MTEX–free and open source software toolbox, in: Solid State Phenomena, Vol. 160, Trans Tech Publ, 2010, pp. 63–68.
[59] S. Bruschi, S. Poggio, F. Quadrini, M. Tata, Workability of Ti-6Al-4V alloy at high temperatures and strain rates, Mater. Lett. 58 (27–28) (2004) 3622–3629.
[60] T. Yao, K. Du, Y. Hao, S. Li, R. Yang, H. Ye, In-situ observation of deformation induced α phase transformation in a β-titanium alloy, Mater. Lett. 182 (2016) 281–284.
[61] A.M. Roy, Multiphase phase-field approach for solid–solid phase transformations via propagating interfacial phase in HMX, J. Appl. Phys. 129 (2) (2021) 025103.
[62] A.M. Roy, Barrierless melt nucleation at solid-solid interface in energetic nitramine octahydro-1, 3, 5, 7-tetranitro-1, 3, 5, 7-tetrazocine, Materialia 15 (2021) 101000.
[63] A.M. Roy, Formation and stability of nanosized, undercooled propagating intermediate melt during $\beta \rightarrow \delta$ phase transformation in HMX nanocrystal, Europhys. Lett. 133 (5) (2021) 56001.
[64] A.M. Roy, Energetics and kinematics of undercooled nonequilibrium interfacial molten layer in cyclotetramethylene-tetranitramine crystal, Physica B 615 (2021) 412986.
[65] A.M. Roy, Influence of nanoscale parameters on solid–solid phase transformation in octogen crystal: Multiple solution and temperature effect, JETP Lett. 113 (4) (2021) 265–272.
[66] A.M. Roy, R. Bose, V. Sundararaghavan, R. Arróyave, Deep learning-accelerated computational framework based on Physics Informed Neural Network for the solution of linear elasticity, Neural Netw. 162 (2023) 472–489.
[67] A.M. Roy, R. Bose, Physics-aware deep learning framework for linear elasticity, 2023, arXiv preprint arXiv:2302.09668.
[68] A.M. Roy, S. Guha, A data-driven physics-constrained deep learning computational framework for solving von Mises plasticity, Eng. Appl. Artif. Intell. 122 (2023) 106049.
[69] A.M. Roy, S. Guha, Elastoplastic physics-informed deep learning approach for j2 plasticity, 2022, Available at SSRN 4332254.